THE EUROPEAN
PHYSICAL JOURNAL A

Regular Article - Experimental Physics

# Investigation of the $\Sigma^0$ Production Mechanism in p(3.5 GeV)+p Collisions

R. Abou Yassine[6,13], O. Arnold[9,10], M. Becker[11], P. Bergmann[5], A. Blanco[1], C. Blume[8], M. Böhmer[10], N. Carolino[1], L. Chlad[14,c], P. Chudoba[14], I. Ciepał[3], J. Dreyer[7], W. Esmail[5], L. Fabbietti[9,10], P. Fonte[1,a], J. Friese[10], I. Fröhlich[8], T. Galatyuk[5,6], J. A. Garzón[15], M. Grunwald[17], M. Gumberidze[5], S. Harabasz[6,b], C. Höhne[5,11], F. Hojeij[13], R. Holzmann[5], H. Huck[8], M. Idzik[2], B. Kämpfer[7,c], B. Kardan[8], V. Kedych[6], I. Koenig[5], W. Koenig[5], M. Kohls[8], J. Kolas[17], G. Korcyl[4], G. Kornakov[17], R. Kotte[7], W. Krueger[6], A. Kugler[14], T. Kunz[10], R. Lalik[4], F. Linz[5,6], L. Lopes[1], M. Lorenz[8], A. Malige[4], J. Markert[5], V. Metag[11], J. Michel[8], A. Molenda[2], C. Müntz[8], M. Nabroth[8], L. Naumann[7], K. Nowakowski[4], J. Orliński[16], J. -H. Otto[11], Y. Parpottas[12], M. Parschau[8], V. Pechenov[5], O. Pechenova[5], K. Piasecki[16], J. Pietraszko[5], A. Prozorov[14,d], W. Przygoda[4], B. Ramstein[13], N. Rathod[17], J. Ritman[5], A. Rost[5,6], A. Rustamov[5,a], P. Salabura[4], N. Schild[6], E. Schwab[5], F. Seck[6], U. Singh[4], S. Spies[8], M. Stefaniak[5,17], H. Ströbele[8], J. Stroth[5,8], C. Sturm[5], K. Sumara[4], O. Svoboda[14], M. Szala[8], P. Tlusty[14], M. Traxler[5], H. Tsertos[12], V. Wagner[14], A. A. Weber[11], C. Wendisch[5], H. P. Zbroszczyk[17], E. Zherebtsova[5,e], M. Zielinski[4], P. Zumbruch[5]

1 LIP-Laboratório de Instrumentação e Física Experimental de Partículas, 3004-516 Coimbra, Portugal
2 Faculty of Physics and Applied Computer Science, AGH University of Science and Technology, 30-059 Kraków, Poland
3 Institute of Nuclear Physics, Polish Academy of Sciences, 31342 Kraków, Poland
4 Smoluchowski Institute of Physics, Jagiellonian University of Cracow, 30-059 Kraków, Poland
5 GSI Helmholtzzentrum für Schwerionenforschung GmbH, 64291 Darmstadt, Germany
6 Technische Universität Darmstadt, 64289 Darmstadt, Germany
7 Institut für Strahlenphysik, Helmholtz-Zentrum Dresden-Rossendorf, 01314 Dresden, Germany
8 Institut für Kernphysik, Goethe-Universität, 60438 Frankfurt, Germany
9 Excellence Cluster 'Origin and Structure of the Universe', 85748 Garching, Germany
10 Physik Department E62, Technische Universität München, 85748 Garching, Germany
11 II. Physikalisches Institut, Justus Liebig Universität Giessen, 35392 Giessen, Germany
12 Department of Physics, University of Cyprus, 1678 Nicosia, Cyprus
13 Laboratoire de Physique des 2 infinis Irène Joliot-Curie, Université Paris-Saclay, CNRS-IN2P3, F-91405 Orsay, France
14 Nuclear Physics Institute, The Czech Academy of Sciences, 25068 Rez, Czech Republic
15 LabCAF. F. Física, Universidade de Santiago de Compostela, 15706 Santiago de Compostela, Spain
16 Uniwersytet Warszawski - Instytut Fizyki Doświadczalnej, 02-093 Warszawa, Poland
17 Warsaw University of Technology, 00-662 Warsaw, Poland

Communicated by Frank Maas

a also at Coimbra Polytechnic - ISEC, Coimbra, Portugal
b also at Helmholtz Research Academy Hesse for FAIR (HFHF), Campus Darmstadt, 64390 Darmstadt, Germany
c also at Technische Universität Dresden, 01062 Dresden, Germany
d also at Faculty of Mathematics and Physics, Charles University, 12116 Prague, Czech Republic
e also at University of Wrocław, 50-204 Wrocław, Poland

a e-mail: hades-info@gsi.de

**Abstract** The production of $\Sigma^0$ hyperons in proton proton collisions at a beam kinetic energy of 3.5 GeV impinging on a liquid hydrogen target was investigated using data collected with the HADES setup. The total production cross section is found to be $\sigma(pK^+\Sigma^0) = 17.7 \pm 1.7(stat) \pm 1.6(syst)$ µb. Differential cross section distributions of the exclusive channel $pp \rightarrow pK^+\Sigma^0$ were analyzed in the center-of-mass, Gottfried–Jackson and helicity reference frames for the first time at the excess energy of 556 MeV. The data support the interplay between pion and kaon exchange mechanisms and clearly demonstrate the contribution of interfering nucleon resonances decaying to $K^+\Sigma^0$. The Bonn–Gatchina partial wave analysis was employed to analyse the data. Due to the limited statistics, it was not possible to obtain an unambiguous determination of the relative contribution of intermediate nucleon resonances to the final state. However nucleon res-

Springer

onances with masses around 1.710 GeV/c$^2$ (N*(1710)) and 1.900 GeV/c$^2$ (N*(1900) or $\Delta$*(1900)) are preferred by the fit.

# 1 Introduction

Strangeness production at intermediate energies in p+p and p+A collisions is of particular importance to the field of hadron physics. The production of baryons with strange quark content, i.e. hyperons, requires creating a new quark flavor, which can occur out of the vacuum from the quark sea in the colliding protons. The production of hyperons is governed by the s-quark mass which is noticeably heavier than the light (u,d) quark flavors.

The resulting (approximate) SU(3) flavor symmetry in the u-d-s sector is a cornerstone of hadron physics. In p+p and p+A collisions, which carry no net strangeness in the entrance channel, the emergence of an s-quark can unravel much of the flavor dynamics in hadronic reactions. The flavor-conserving strong interaction process requires associated strangeness production, which can be realized by the simultaneous creation of a single-strange hyperon, such as $\Lambda$ or $\Sigma^0$, and an associated kaon. Strangeness in the early Universe is of significant importance as it provides insights into the particle composition during the hadron epoch and helps in understanding the nonequilibrium processes that are prerequisites for time-dependent processes in the Hubble expanding Universe. Furthermore, it potentially offers alternate opportunities for baryogenesis, thereby contributing to our understanding of the Universe's evolution and the fundamental laws of physics [1]. In addition, understanding the production mechanism of strange baryons near threshold deepens our knowledge of their internal structure and of the strong interaction in the non-perturbative regime. Strangeness production also serves as a probe to study hot and dense nuclear matter in heavy ion collisions [2].

The production of the $\Lambda$ hyperon in p+p and p+A reactions near threshold has been studied extensively by many experiments including HADES [3–7], yet there are only few experimental investigations on the $\Sigma^0$ hyperon [3,8]. Although there have been many dedicated theoretical investigations and significant experimental results, the strangeness production mechanism remains poorly understood. In the context of the boson exchange model [9–12], it is assumed that the initial protons exchange a virtual meson. The interaction between the meson and the initial protons results in the production of the final state particles, which can proceed directly or via an intermediate resonance.

The exchange of a virtual meson can be put into one of two categories. The first category is strange meson exchange, where strangeness exchange occurs, and no resonances are involved. In this case, the reaction amplitude KN $\rightarrow$ KN is governed by t-channel diagrams. The second category is non-strange meson exchange, a pion exchange in its simplest form. At the same time the elementary reaction amplitude $\pi$N $\rightarrow$ KY is dominated by resonance excitations, which implies a strong and characteristic energy dependence, where Y stands for hyperons ($\Lambda$, $\Sigma^0$,...).

Several experiments have studied the exclusive reaction pp $\rightarrow$ pK$^+\Lambda$ and proven that a pure phase space model description of the data is not sufficient without taking the dynamics of the process into account [3,7,13,14]. It was found that the $\Lambda$ hyperon production is dominated by the excitation and subsequent decay of N* resonances to the K$^+\Lambda$ decay channel. In particular N*(1650) (J$^P$= $\frac{1}{2}^-$), N*(1710) (J$^P$= $\frac{1}{2}^+$) and N*(1720) (J$^P$= $\frac{3}{2}^+$) were found to contribute. This supports a picture wherein the exchange of non-strange mesons is the leading process in the production mechanism. In addition, a considerable Final State Interaction (FSI) was found to contribute [15,16] leading to $\Sigma$N $\rightarrow$ $\Lambda$N conversion that is observed as a $\Sigma$N cusp effect in the $\Lambda$ cross section [17]. In the pp $\rightarrow$ pK$^+\Sigma^0$ reaction the proton-hyperon FSI seems to be negligible, especially at low energies near threshold and a pure phase space distribution describes the data reasonably well. The cross section ratio $\sigma$(pK$^+\Lambda$) / $\sigma$(pK$^+\Sigma^0$) below excess energies of $\sim$ 20 MeV is about 28 in agreement with the SU(6) prediction and reduces drastically to about 2.5 at excess energies above 300 MeV [18,19]. This energy-dependence of the cross section ratio is strongly affected by FSI effects in the pp $\rightarrow$ pK$^+\Lambda$ reaction [20].

Besides the energy dependence of the cross section, the differential cross sections at selected energies add much more stringent tests of the model descriptions. This study fills this gap and delivers such data which allow some clues about the involved exchange mesons and resonances, in particular by employing a partial wave analysis.

Furthermore, a theoretical study of the reaction pp $\rightarrow$ pK$^+\Sigma^0$ based on a chiral dynamical study has been proposed in [21]. This approach uses the pion and kaon exchange mechanisms and chiral amplitudes. In addition, the model allows each two body combination in the final state to undergo FSI. The contribution of nucleon resonances appears naturally using chiral unitary amplitudes.

This paper is organized as follows. In Sect. 2, the experimental setup is briefly explained. Section 3 is devoted to the $\Sigma^0$ selection method, where the particle identification, the $\Lambda$ hyperon reconstruction and the kinematic refit methods are presented. In Sect. 3.5 the method for efficiency correction and differential analysis is described. Sections 5 and 6 present the calculated total production cross section and the partial wave analysis of the exclusive reaction pp $\rightarrow$ pK$^+\Sigma^0$. In Sect. 7 a summary and a short outlook are given.

## 2 The HADES experiment

The data presented in this article were collected in April 2007 with the High Acceptance Di-Electron Spectrometer (HADES) located at the heavy ion synchrotron SIS18, at GSI Helmholtzzentrum für Schwerionenforschung in Darmstadt, Germany. HADES, as shown in Fig. 1, is characterized by six identical sectors covering almost the full azimuthal range and polar angles from $\theta = 18°$ to $\theta = 85°$. Each sector of the spectrometer contains a Ring-Imaging Cherenkov Detector (RICH) operating in a magnetic field-free region that allows lepton identification over a wide range of momenta. Two Multi-Wire Drift Chambers (MDCs) are placed in front of a toroidal magnetic field, and two outer MDCs are placed behind the magnetic field. The MDCs enable the momentum information and the specific energy loss dE/dx to be reconstructed for each particle track. Two scintillator hodoscopes, the Time Of Flight (TOF) and TOFino, are positioned behind the magnet and provide a stop time ($t_s$) signal. The TOF system covers polar angles from 44° to 88° and has a time resolution of $\sigma_{TOF} = 150$ ps. TOFino, in contrast, is a low-granularity system that measures at polar angles smaller than 45°. However, its time resolution is less precise, at about $\sigma_{TOFino} = 420$ ps. Both systems serve as inputs to the trigger systems that initiate the data readout. For a detailed description of the HADES setup, see [22].

In the present analysis, a proton beam with an intensity of $10^7$ particles/s and kinetic energy T = 3.5 GeV was incident on a liquid hydrogen target with an areal density of 0.35 g/cm$^2$. The dimensions of the target were 15 mm in diameter and 50 mm length located between −65 to −15 mm in the longitudinal direction. The data readout was started by a first level trigger requiring a charged particle multiplicity ≥ 3

(M3). In total, $1.14 \times 10^9$ events were recorded under these conditions [4].

During this experiment HADES included an additional Forward Wall (FW) scintillator hodoscope that was placed 7 ms downstream the target in a magnetic field-free region and covered polar angles from $\theta = 0.33°$ to $\theta = 7.17°$ with full azimuthal acceptance. The FW measured the hit position and arrival time of the particle track with a time resolution of about 700 ps [23].

## 3 Event selection method

In this section, the exclusive reconstruction of the reaction $pp \to pK^+\Sigma^0$ is presented. The $\Sigma^0$ hyperon is reconstructed via its electromagnetic decay $\Sigma^0 \to \Lambda\gamma$ (BR ≈ 100%) and the daughter $\Lambda$ hyperon is reconstructed with the decay mode $\Lambda \to p\pi^-$ (BR = 63.9%).

The $\Sigma^0$ reconstruction strategy includes the following steps: (a) time of flight ($tof$) reconstruction, (b) charged particle identification (PID), (c) the $\Lambda$ hyperon reconstruction, and (d) the $\Sigma^0$ hyperon reconstruction.

### 3.1 Time of flight reconstruction

The interaction of the high intensity proton beam with the START detector induced a background and prevented a stable operation of the RICH detector. Therefore, it was not possible to use the START detector information during this experiment. Consequently, the $tof$ of particle tracks were not directly measured since there was no common start time ($t_0$) reference for tracks in the same event. The start time has to be reconstructed in order to obtain a proper time of flight measurement.

**Fig. 1** Schematic cross-sectional view of the HADES, including the forward wall. Adapted from [22]
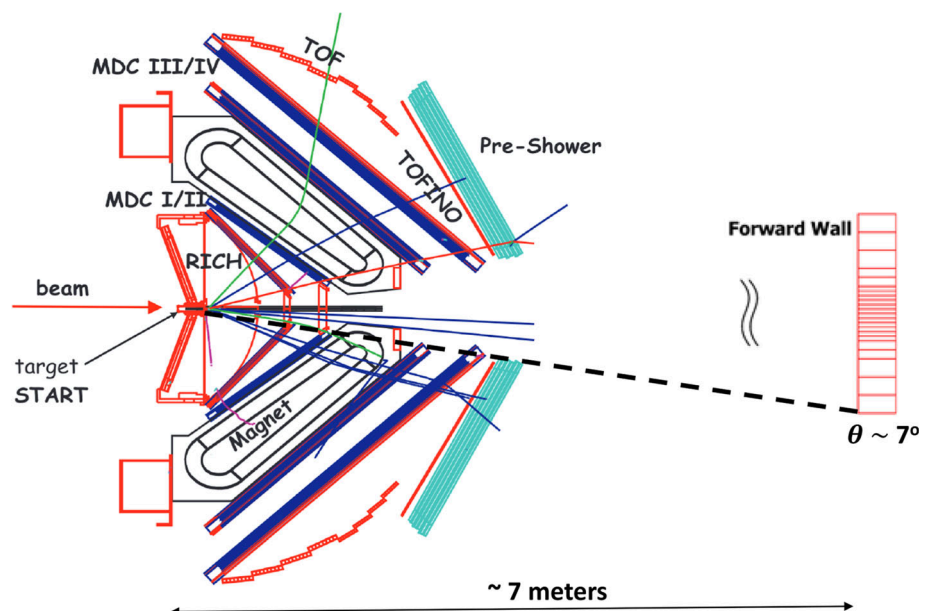
The reconstruction algorithm is based on the assumption that at least one particle has been correctly identified. Since pions are abundantly produced, it is assumed that any negatively charged particle track that is geometrically uncorrelated to a ring in the RICH detector is a $\pi^-$. The common start time for each event is calculated by

$$t_0 = t_s - \frac{d}{c}\left(\frac{\sqrt{p^2 + m_\pi^2 c^2}}{p}\right) , \tag{1}$$

where $t_s$ is the stop time of the $\pi^-$, $d$ is the track length to the TOF or TOFino hit, $m_\pi$ is the pion mass, $p$ is the momentum of the $\pi^-$ and $c$ is the velocity of light. The *tof* of the other particles in the same event is the difference between the measured stop time $t_s$ and the common start time $t_0$.

### 3.2 Particle identification (PID)

The reconstruction of the exclusive reaction $pp \to pK^+ p\pi^- \gamma$ only requires the identification of three particle species, pions ($\pi^-$), kaons ($K^+$) and protons (p), since the event is kinematically complete even without measuring the photon ($\gamma$).

As mentioned in the previous section, the $\pi^-$ is identified as any negatively charged track that is geometrically uncorrelated to a ring in the RICH detector. Therefore, the problem reduces to identifying the positively charged tracks.

The developed algorithm for this study is based on deep learning techniques because of their capability to model complex and non-linear data relationships. Specifically, an autoencoder neural network inspired by the M2 model proposed by Kingma et al. in [24] was implemented using the PyTorch framework [25]. In order to avoid the discrepancies between the simulation and real data distributions, the model is trained simultaneously with both simulated and real events. The auto-encoder learns the combined features of both real and simulated events and compress it to a bottleneck layer (latent space), where the differences between real data and simulations are no longer visible. On top of the bottleneck layer, a classification layer has been stacked, which has three output nodes corresponding to the three classes ($\pi^+$, $K^+$ and p). Each node outputs a number between 0 and 1, where all numbers sum to 1, so that each number can be interpreted as a probability of being a specific particle type. The network is trained by minimizing a binary cross-entropy cost function [26].

The input features used to train the auto-encoder are the momentum components, the energy loss dE/dx in the MDC and TOF sub-systems, the reconstructed *tof* and the distance to the TOF/TOFino hit.

The classification accuracy evaluated on a holdout dataset is 92% for pions, 76% for kaons, and 98% for protons. The noticeably lower classification accuracy for kaons is due to their suppressed production rate compared to protons and pions within this energy range. Additionally, pions were misidentified as kaons 10% of the time and as protons 5% of the time. A more detailed description of the model performance can be found in [27].

### 3.3 Λ hyperon reconstruction

The next step after the PID is to reconstruct the intermediate Λ hyperon. In this analysis the Λ reconstruction method is two-fold. In the first case, which is referred to as the *Spectrometer data-set*, events with exactly 2 protons, 1 pion and 1 kaon are required to be within the main HADES detector acceptance. The other case, referred as the *WALL data-set*, events were accepted if exactly 1 proton, 1 pion and 1 kaon are registered in HADES and in addition one hit in the FW. In the latter case, it is assumed that the hit registered in the FW is due to the daughter proton from the Λ decay (marked as $p_{decay}$).

A common primary vertex in each event is then defined as the intersection point or the Point of Closest Approach (PCA) of the proton and kaon tracks. Since there is more than one proton in each event in the *Spectrometer data-set*, the proton-kaon pair with the smaller Distance of Closest Approach (DCA) is used to define the primary vertex. To reduce the contribution from off-target events, a two dimensional selection is applied on the primary vertex position $(x, y, z)$:

(a) $-65\,\mathrm{mm} < z < -15\,\mathrm{mm}$  and
(b) $\sqrt{x^2 + y^2} < 5\,\mathrm{mm}$.

The Spectrometer data-set

Since the daughter Λ decays weakly ($c\tau = 7.89$ cm), it can be identified by its displaced vertex. First, all possible combinations of the two p and $\pi^-$ candidates were made, leaving the decision about which is the decay proton ($\Lambda \to p\pi^-$) for later. For each combination the decay vertex (the displaced vertex) is defined as the PCA between the two tracks. The DCA between the p and $\pi^-$ tracks (marked as $d_{p\pi^-}$) is expected to be small if the tracks stem from the same vertex. Therefore, an upper limit of $d_{p\pi^-} < 10\,\mathrm{mm}$ is imposed in order to reduce Combinatorial Background (CB), which originates from combining the wrong p and $\pi^-$ pairs. Considering momentum and energy conservation, the p should be emitted in nearly the same direction as the Λ in the laboratory reference frame, while the $\pi^-$ will have a different direction. Thus, the DCA between the p track and the primary vertex ($d_{p,pvtx}$) is required to be smaller than the DCA between the $\pi^-$ track and the primary vertex ($d_{\pi^-,pvtx}$). Finally, the DCA between the calculated Λ track and the primary vertex ($d_{\Lambda,pvtx}$) is required to be < 6 mm. The distributions of the
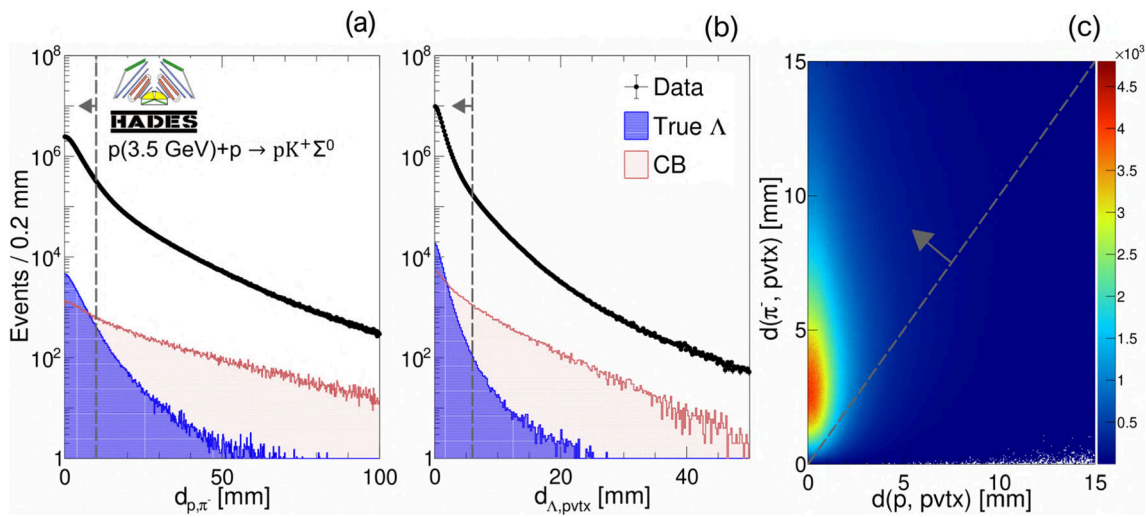
**Fig. 2** **a** The DCA distribution between the p and $\pi^-$ tracks. **b** The DCA distribution between the $\Lambda$ track and the primary vertex. In both panels, data are shown by the black points, the blue histogram represents the true $\Lambda$ and the red histogram represents the CB, where both the true $\Lambda$ and the CB were estimated from the simulation. **c** Distribution of the DCA between the $\pi^-$ track and the primary vertex as a function of the DCA between the p track and the primary vertex. The arrows indicate the accepted regions

topological variables are shown in Fig. 2, where the selection criteria are indicated by the vertical dashed lines. The proton used in the $\Lambda$ reconstruction is tagged as the decay proton (marked in the following as $p_{decay}$), while the other proton in the event is tagged as the scattered (primary) proton.

To further purify the selected $\Lambda$ sample, the event kinematics were constrained to the $\Sigma^0$ production range. The squared $p\Lambda$ missing mass ($MM^2(pp_{decay}\pi^-)$) is required to be $> 0.2$ $GeV^2/c^4$ in order to reject the multi-pion production channel as shown in Fig. 3. In this figure, the experimental data are shown by the black points and the simulations (discussed in Sect. 3.4) by different colored histograms. Two peaks are visible, the first peak at 0.02 $GeV^2/c^4$ corresponds to the multi-pion channel via the reaction $pp \rightarrow pp\pi^+\pi^-$ (violet histogram), where a $p\pi^-$ pair is incorrectly identified as a $\Lambda$ candidate and the $\pi^+$ is incorrectly identified as a $K^+$. The other broader peak is the sum of $pp \rightarrow pK^+\Lambda$, $pp \rightarrow pK^+\Sigma^0$ and $pp \rightarrow pK^+\Lambda\pi^0$ reactions shown by the red, blue and green histograms, respectively. The relative normalizations of the simulated channels have been chosen to best fit the experimental data as explained in Sect. 3.4.
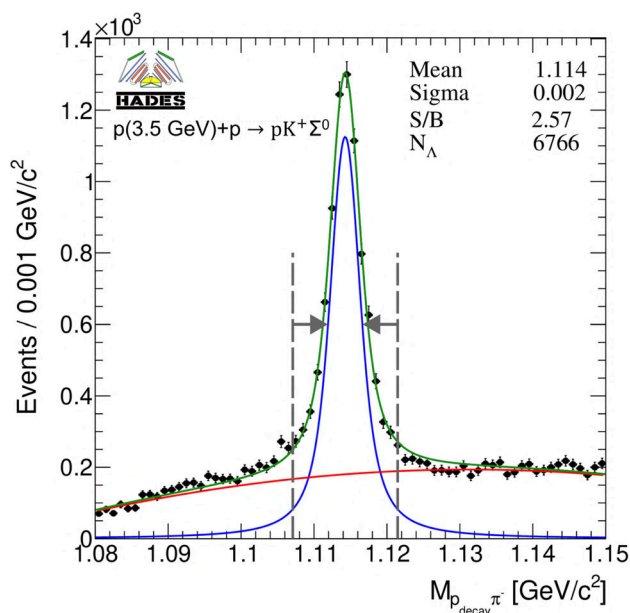
The $p_{decay}\pi^-$ invariant mass distribution is shown in Fig. 4. A peak around the nominal $\Lambda$ mass is visible on top of background. The signal has been parameterized by a Voigt distribution and the background is modeled by a fourth-order polynomial. Events are further processed if they are in the range of $\mu \pm 3\sigma$, where the calculated signal to background ratio in this range is $S/B = 2.57$ and the number of $\Lambda$ candidates is $N_\Lambda = 6766$.
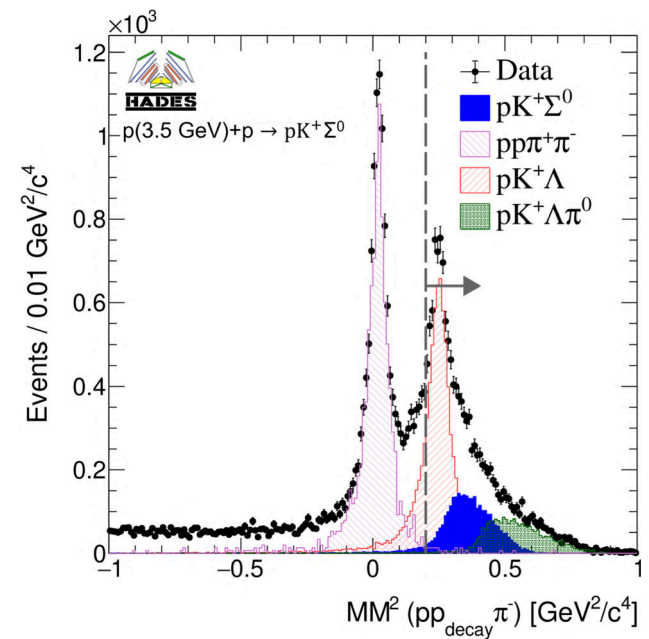


**Fig. 3** The squared $pp_{decay}\pi^-$ missing mass distribution after applying the topological selections. Black points are the *Spectrometer data-set* data. The violet histogram is the $pp \rightarrow pp\pi^+\pi^-$ simulation. The $pp \rightarrow pK^+\Lambda$, $pp \rightarrow pK^+\Sigma^0$ and $pp \rightarrow pK^+\Lambda\pi^0$ simulations are shown by the red, blue and green histograms, respectively. The vertical line and the arrow indicate the accepted region for the further analysis

The WALL data-set

In the *WALL data-set* the hit in the FW is assumed to be due to the decay proton. Since the FW is installed in a magnetic

**Fig. 4** The $p_{decay}\pi^-$ invariant mass distribution. The vertical dashed lines indicate the selected mass range. The blue, red and green curves are for the signal, background and the total fit

field-free region, the $p_{decay}$ is reconstructed as a straight line trajectory from the primary vertex position to the hit in the FW. The track momentum is calculated from the *tof* and the distance from the primary vertex and the FW detector hit, assuming the proton mass. In this case, the topological cuts are not as effective to suppress the background as in the *Spectrometer data-set*. Therefore, events fulfilling the following kinematical constraints were selected:

(i) $MM^2(pp_{decay}\pi^-) > 0.2$ GeV$^2$/c$^4$ (Fig. 5a) and
(ii) The squared missing mass of all charged particles is required to be in the following range:
$-0.02$GeV$^2$/c$^4$ < $MM^2(pK^+p_{decay}\pi^-)$ < $0.01$GeV$^2$/c$^4$ because only a photon is missing to completely measure the exclusive final state (Fig. 5b).

The $p_{decay}\pi^-$ invariant mass distribution for the *WALL data-set* is shown in Fig. 6 after applying the selections mentioned above. Once again, the peak has been fitted by a Voigt distribution and the background by a fourth-order polynomial. However, the mass resolution of the $\Lambda$ peak of the *Spectrometer data-set* (Fig. 4) is better than the signal of the *WALL data-set* (Fig. 6), since in the latter case the proton was detected in the FW, which has a worse momentum resolution. Events are further processed if they are in the range of $\mu \pm 3\sigma$, where the calculated signal to background ratio in this range is S/B = 1.56 and the number of $\Lambda$ candidates is $N_\Lambda = 2340$.

### 3.4 $\Sigma^0$ hyperon reconstruction

To further suppress the remaining background and to obtain a better mass resolution, a kinematic fit based on the Lagrange multiplier method is employed [28]. The fit $\chi^2$, expressed as

$$\chi^2(\eta, \lambda) = (y - \eta)^T V(y)(y - \eta) + 2\lambda^T f(\eta) , \qquad (2)$$

is minimized by differentiating $\chi^2$ with respect to all measured variables. Here $y$ is a vector containing the initial guesses for the measured quantities, which are the track parameters provided by the tracking algorithm, $\eta$ is an improved set of the track parameters and $V$ is the covariance matrix comprising the estimated errors on the measured quantities. The constraint equations are expressed as a function of $\eta$ in $f(\eta)$, where $\lambda_i$ form a set of Lagrange multipliers.

The spherical coordinates used in this analysis for the track parameterization are defined as follows

$$y = \begin{bmatrix} 1/p \\ \theta \\ \phi \end{bmatrix} , \qquad (3)$$

where $1/p$ is the inverse of the absolute momentum measured in GeV$^{-1}$c, $\theta$ and $\phi$ are the polar and azimthual angles of the track measured in radians.

Two constraints were applied to both data-sets. The first is the proton and pion from the $\Lambda$ decay are constrained to the $\Lambda$ mass ($M_\Lambda = 1.1157$ GeV$^2$/c$^4$). The second constraint is that the missing mass of all the charged final state particles is constrained to the photon mass ($M_\gamma = 0$ GeV$^2$/c$^4$).

The probability that a $\chi^2$ of the theoretical distribution is greater than or equal to the $\chi^2$ value found from the fit is known as the p-value ($P(\chi^2)$). The p-value distributions of the *Spectrometer* and the *WALL* data-sets are shown in Fig. 7. Because both $\Lambda$ and $\Sigma^0$ have MM($pK^+\Lambda$) = 0, they have similar distributions, which makes these two reactions difficult to distinguish. On the other hand, the reaction pp $\rightarrow$ $pK^+\Lambda\pi^0$ should ideally have zero p-value. However, due to the limited detector resolution it has p-values greater than zero, which is more pronounced in the *WALL* data-set. The signal events show an almost flat distribution between 0 and 1, while events that do not satisfy the constraint equations have a prominent yield of p-values close to 0. Therefore, events with P($\chi^2$) > 0.01 are selected, where the cut was optimized based on a significance analysis.

Simulation scaling to the experimental data

By inspecting the $pK^+$ missing mass distribution of the combined data-set shown in Fig. 8, two peaks corresponding to the $\Lambda$ and the $\Sigma^0$, as well as other minor contributions in the high mass region, are plainly evident. In order to quantify the different contributions an incoherent cocktail has been
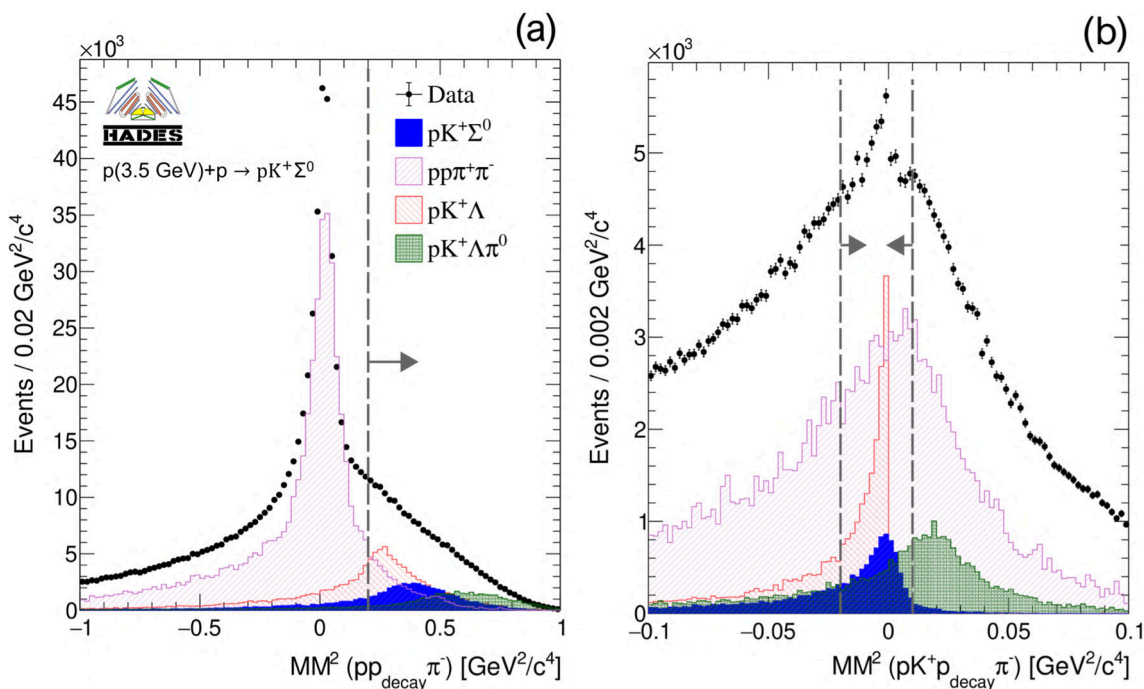
**Fig. 5 a** The squared $pp_{decay}\pi^-$ missing mass distribution of *WALL data-set*. **b** The squared $pp_{decay}\pi^- K^+$ missing mass distributions. The $pp \to pp\pi^+\pi^-$, $pp \to pK^+\Lambda$, $pp \to pK^+\Sigma^0$ and $pp \to$ $pK^+\Lambda\pi^0$ simulations are shown by the violet, red, blue and green histograms, respectively. The arrows indicate the accepted regions
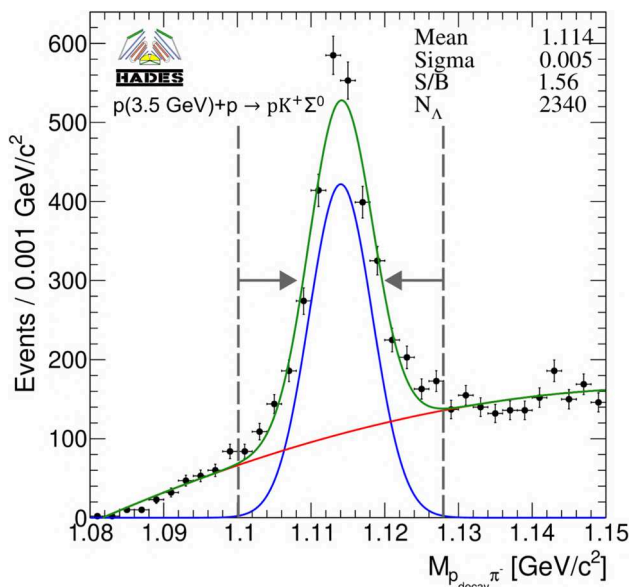


**Fig. 6** The $p_{wall}\pi^-$ invariant mass distribution. The vertical dashed lines indicate the selected mass range. The blue, red and green curves are for the signal, background and the total fit

simulated using the Pluto event generator [29]. All the simulated reactions have been processed using the same full scale analysis employed for the experimental data, thus taking into account the efficiency of the trigger condition, the tracking algorithm and the analysis procedure. The particle decays, the acceptance and the particle interactions with the materials of HADES and the FW have been considered by using GEANT3 [30].

To determine the contributions of the different channels, a fit of the simulations to the measured missing mass spectrum $(MM(pK^+))$ has been carried out by minimizing the quantity

$$\chi^2 = \sum_i^{n_{bins}} \frac{(n_{data} - \sum_{ch}(f^{ch} n^{ch}_{simulation}))^2}{\sigma^2_{data} + \sigma^2_{simulation}}, \quad (4)$$

where the summation runs over the number of bins of the missing mass spectrum, $n_{data}$ is the number of data events in each bin, $n^{ch}_{simulation}$ is the number of simulated events in each bin for each channel and $f^{ch}$ is a scaling factor for each channel. The uncertainty for the data and the simulations in each bin is $\sigma_{data}$ and $\sigma_{simulation}$, respectively.

As can be seen from Fig. 8, the experimental data is primarily described by contributions of $pp \to pK^+\Lambda$, $pp \to pK^+\Sigma^0$ and $pp \to pK^+\Lambda\pi^0$ indicated by the red, blue and the green histogram, respectively. The other simulated channels have minor contributions. In total 2613 $\Sigma^0$ candidates were collected within the $pK^+$ missing mass range of $1.170-1.220\,\mathrm{GeV}^2/c^4$, 58% of them are within the main HADES acceptance and 42% within the FW acceptance. The signal purity in the mass window calculated from
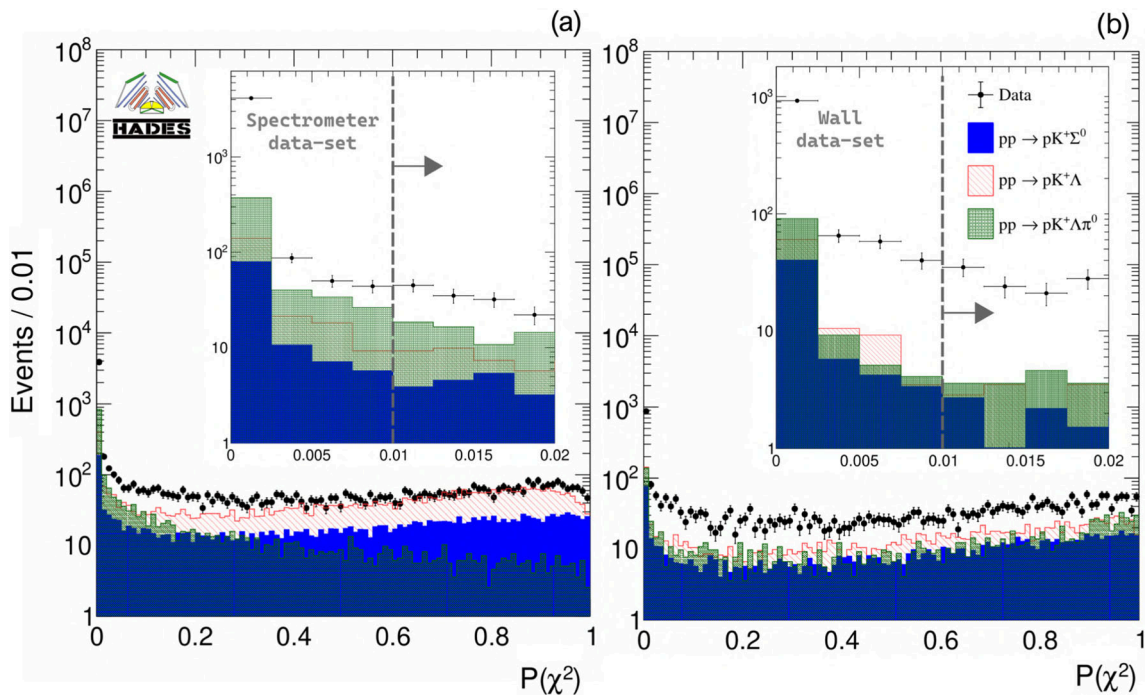
**Fig. 7 a** The p-value distributions for the HADES data-set and for **b** the WALL data-set. The insets display the region of small p-values, where the dashed line and the arrow indicates the accepted region. The

$pp \rightarrow pK^+\Lambda$, $pp \rightarrow pK^+\Sigma^0$ and $pp \rightarrow pK^+\Lambda\pi^0$ simulations are shown by the red, blue and green histograms, respectively
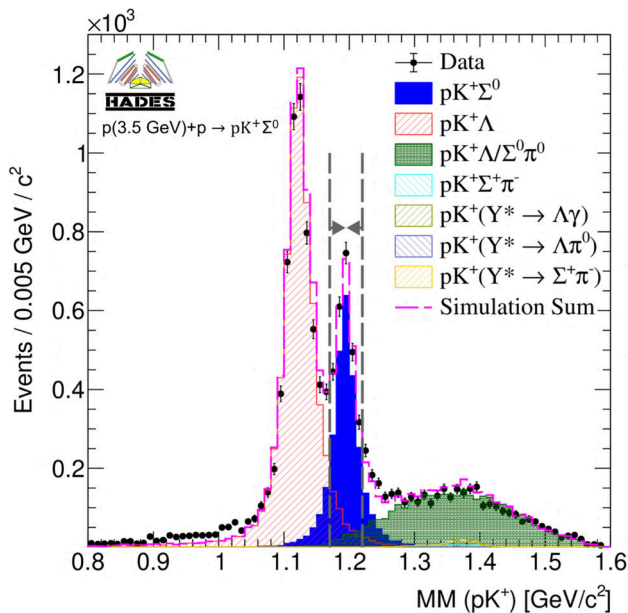


**Fig. 8** The $pK^+$ missing mass distribution. The colored histograms represent the simulated channels, where Y* refers to an excited hyperon ($\Sigma(1385)$, $\Lambda(1405)$ or $\Lambda(1520)$). The two peaks are due to the exclusive reactions $pp \rightarrow pK^+\Lambda$ and $pp \rightarrow pK^+\Sigma^0$ as shown by the red and the blue histograms, respectively. The vertical dashed lines mark the mass window used to select candidate events of the $pp \rightarrow pK^+\Sigma^0$ final state

the simulation is found to be 81%, where the main background contributions are the reactions $pp \rightarrow pK^+\Lambda$ (14%) and $pp \rightarrow pK^+\Lambda\pi^0$ (5%).

### 3.5 Efficiency and acceptance correction

The rate of production of three particles final state is governed by four independent kinematic variables for an initial state without transverse polarization. Thus, a model-independent correction procedure needs to be performed in four-dimensions simultaneously. However, This approach is not practical since it requires a huge number of events to populate each phase space bin with sufficient statistics. Moreover, the HADES experiment does not provide full coverage in all phase space bins. Therefore, a purely model-independent correction is challenging. However, to address this issue, we employ the partial wave analysis (discussed in Sect. 6), which has demonstrated a robust capacity to describe data within the HADES acceptance effectively. This is accomplished by using a simulated phase space distribution, with each event assigned a weight determined by the best partial wave solution. These weighted events are then processed through a full-scale simulation and analysis.

A one-dimensional correction matrix, denoted as $R$, is then defined by the equation $R = M/T$. Here, $T$ represents the initial $4\pi$ distribution, while $M$ denotes this distribu-
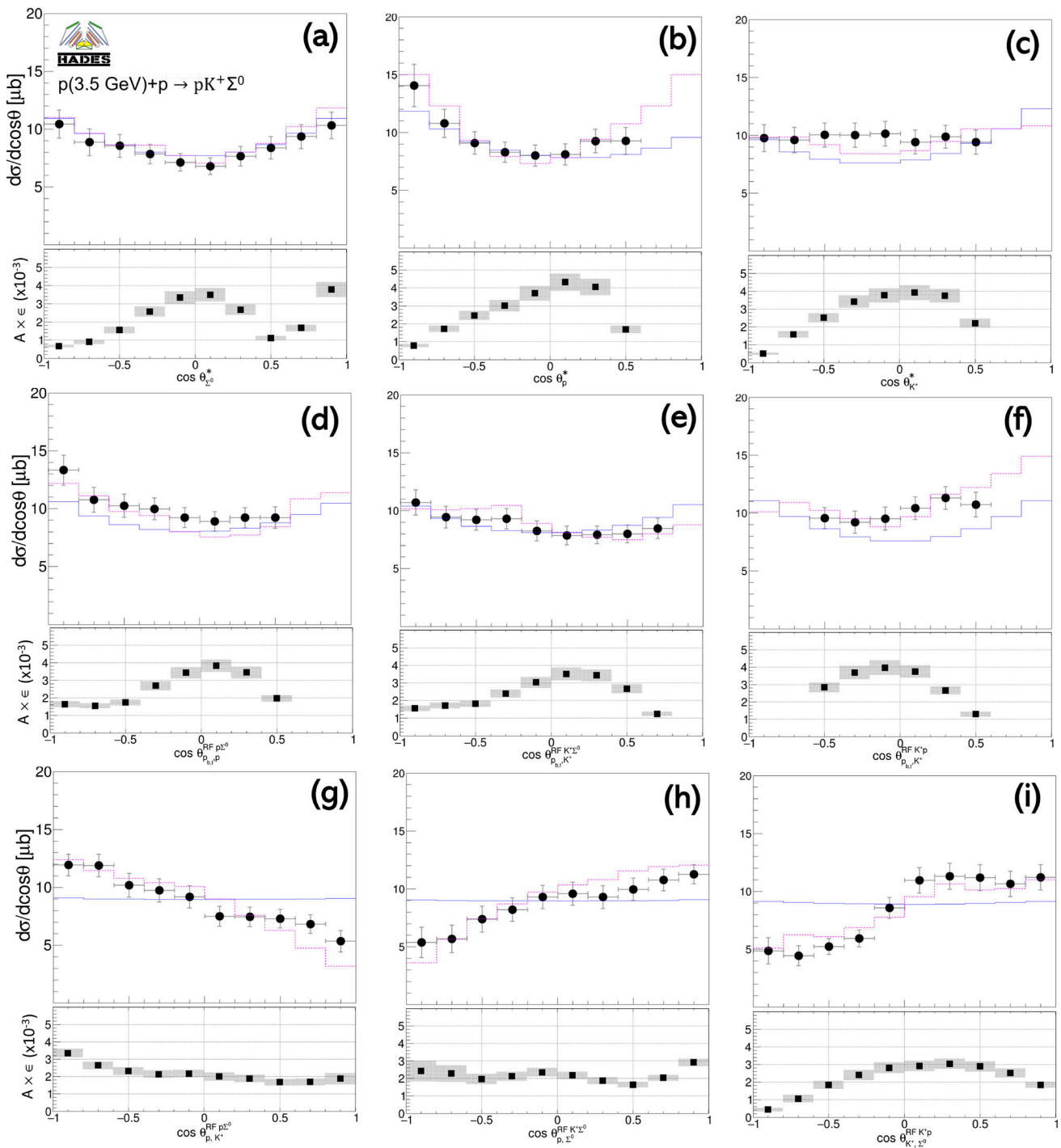
**Fig. 9** The corrected angular distributions in the CMS (top row), Gottfried-Jackson (middle row) and helicity frames (bottom row). The experimental data are shown by the black points, where the error bars are the square root of the quadratic sum of the statistical and systematic uncertainties. The blue histogram represent the weighted $pp \rightarrow pK^+\Sigma^0$ phase space simulation described in the text and the dotted pink histogram indicates the best partial wave analysis solution (discussed in Sect. 6). Below each of the angular distributions is the product of the efficiency and acceptance

tion after it has been processed through a full-scale simulation and analysis. Consequently, a unique correction matrix $R = M/T$ is constructed for each specific angular distri-

bution shown in Fig. 9. A representation of the product of acceptance and efficiency ($A \times \epsilon$) is shown below each angular distribution in Fig. 9, where the average value was found

to be approximately $2.4 \times 10^{-3}$. Furthermore, the structure of the FW is distinctly visible in the $\cos\theta_{\Sigma^0} > 0.6$ forward region, as shown in Fig. 9 (a). Here, the $\Lambda\,(\Sigma^0 \to \Lambda\gamma)$ is partially reconstructed in the FW. However, this is not the case for $\cos\theta_p^*$ and $\cos\theta_{K^+}^*$, as the primary proton and the kaon are detected only in HADES.

### 3.6 Absolute normalization and systematic uncertainties

The production cross section of $\Sigma^0$ ($\sigma_{\Sigma^0}$) can be calculated by normalizing the corrected $\Sigma^0$ yield to the p+p elastic scattering yield measured in the same experimental run, as described in [31]. This is given by the formula:

$$\sigma_{\Sigma^0} = \left(\frac{\sigma^{elastic}pp}{N^{elastic}pp}\right) N_{\Sigma^0}\,, \tag{5}$$

where $\sigma^{elastic}pp$ is the cross section for p+p elastic scattering, $N^{elastic}pp$ is the number of reconstructed p+p elastic events corrected for acceptance and efficiency and $N_{\Sigma^0}$ is the number of corrected $\Sigma^0$ events.

This normalization results in a systematic uncertainty of 7%. Additionally, the systematic error associated to the event selection has been estimated by varying the selection ranges and recalculating the cross section.

To evaluate the effect of different selection cuts on the calculated cross section (see Sect. 5), the entire analysis chain was repeated numerous times using various cut combinations. Each cut was varied in two steps in either direction. The cross section for each combination was then calculated by integrating the yield of the $\cos\theta_{\Sigma^0}^*$ angular distribution. Following this approach, the resulting systematic error, defined as the $1\sigma$ interval of the cross section distribution, was found to be approximately 2%.

Another contributor to the systematic errors is the PID, which was assessed using the dropout layers of the neural network during inference time, which is equivalent to a Bayesian approximation [32]. The estimated magnitude of the PID systematic error is approximately 5%.

## 4 Angular distributions

This section presents the differential cross section of the reaction pp $\to$ pK$^+\Sigma^0$, namely the angular distributions of final state particles in the center of mass (CMS) frame, as well as in both the Gottfried–Jackson and helicity frames of all two-body subsystems. All distributions are acceptance and efficiency corrected and then fit with Legendre polynomials $d\sigma/d\cos\theta = \sum_l A_l \cdot P_l$, with $l = 0, 1, 2$. The coefficients $A_1$ and $A_2$ are used to judge the asymmetries and anisotropies of the observed distributions. The best description of the distribution (indicated by the blue histogram in Fig. 9) was found

when the simulations have been weighted simultaneously with the angular distribution of the $\Sigma^0$ hyperon in the CMS frame and the proton Gottfried-Jackson angular distribution measured in the p$\Sigma^0$ rest frame obtained from the data.

### Center of mass frame

The angular distributions of the three final state particles in the CMS are shown in the top row of Fig. 9. The Legendre polynomial coefficients obtained from the fits of the angular distributions are listed in Table 1. Since the initial p+p is a symmetric system, the $A_1$ Legendre parameters of all CMS distributions were set to zero. The angular distribution of the $\Sigma^0$ hyperon (Fig. 9a) and proton (Fig. 9b) shows an anisotropy, where it is more pronounced for the proton as quantified by the $A_2$ parameter listed in Table 1. From the observed anisotropies and the fit parameters one deduces that a non-zero orbital angular momentum ($L$) is observed in both the $p - K^+\Sigma^0$ and $\Sigma^0 - pK^+$ sub-systems. This is in contrast to the kaons, where the angular distribution is compatible with isotropy. For pure pion exchange, the final state proton is the leading particle, since the exchange pion has a small mass, implying a small 4-momentum transfer so that the proton is preferably emitted in the direction of the initial protons, which could explain the anisotropy in the proton angular distribution. In this picture, the $\Sigma^0$ CMS angular distribution reflects the proton one, while the kaon has a broader distribution.

The angular distributions in the overall CMS are not suited to directly draw conclusions on resonant production, which proceeds as a two step process pp $\to$ pR, R $\to$ K$^+\Sigma^0$, where R stands for every kind of nucleon resonance, that can be either an isospin 1/2 N$^*$ state or an isospin 3/2 $\Delta^*$ state. Therefore in the following the Gottfried-Jackson and helicity frames are presented as a more natural choice for the Lorentzian reference frames in order to study the reaction properties due to resonant production.

### Gottfried–Jackson frames

The Gottfried–Jackson (G–J) frame first introduced in [33] is the rest frame of two out of the three produced particles. In the G–J frame, the G-J angle is defined as the angle between one of the rest frame particles (e.g. the $\Sigma^0$) and the initial proton $\theta_{p_{b,t},\Sigma^0}^{RF\ K^+\Sigma^0}$, where the label RF stands for reference frame, the superscript indicates which rest frame is used and the subscript stands for the two particles, between which the angle is measured. It should be noted that the two initial protons are indistinguishable. Therefore, the angular distribution is calculated by using the angle to both protons ($p_{b,t}$).

In the case of kaon (pion) exchange, the K$^+$p (K$^+\Sigma^0$) rest frame is equivalent to the rest frame of the exchanged meson

**Table 1** Coefficients of Legendre polynomials determined by fitting the angular distributions presented in Fig. 9

| Angle | $A_0$ [μb] | $A_1$ [μb] | $A_2$ [μb] |
|---|---|---|---|
| $\cos\theta^*_{\Sigma^0}$ | $8.55 \pm 0.31$ | $0.00$ | $2.75 \pm 0.73$ |
| $\cos\theta^*_p$ | $10.01 \pm 0.50$ | $0.00$ | $4.33 \pm 1.27$ |
| $\cos\theta^*_{K^+}$ | $9.83 \pm 0.43$ | $0.00$ | $-0.13 \pm 1.02$ |
| $\cos\theta^{FRp\Sigma^0}_{p_{b,t},p}$ | $10.40 \pm 0.80$ | $-0.64 \pm 1.73$ | $2.79 \pm 1.85$ |
| $\cos\theta^{FRK^+\Sigma^0}_{p_{b,t},K^+}$ | $8.55 \pm 0.71$ | $-1.61 \pm 1.54$ | $0.66 \pm 1.63$ |
| $\cos\theta^{FRK^+p}_{p_{b,t},K^+}$ | $10.30 \pm 1.00$ | $1.91 \pm 1.18$ | $0.50 \pm 2.69$ |
| $\cos\theta^{FRK^+\Sigma^0}_{p,\Sigma^0}$ | $8.70 \pm 0.30$ | $3.17 \pm 0.59$ | $-0.73 \pm 0.75$ |
| $\cos\theta^{FRp\Sigma^0}_{p,K^+}$ | $8.75 \pm 0.29$ | $-3.52 \pm 0.50$ | $0.37 \pm 0.67$ |
| $\cos\theta^{FRK^+p}_{K^+,\Sigma^0}$ | $8.81 \pm 0.31$ | $4.84 \pm 0.56$ | $-0.98 \pm 0.75$ |

and the initial proton. In this way, the initial $2 \to 3$ reaction is reduced to a pure $2 \to 2$ reaction. If there is a resonant production, the internal angular momentum of the resonance is then reflected in this observable. It has to be noted that the distributions in the G–J frames do not have to be symmetric. The reason is the asymmetric reaction system, where either a kaon or a pion collides with a proton. The angular distributions in the G–J frames are shown in the middle row of Fig. 9.

An anisotropy is observed in the $p\Sigma^0$ G–J frame (Fig. 9d), which could be due to a relative angular momentum in the $p\Sigma^0$ system. This effect is related to the above mentioned anisotropies of the p and $\Sigma^0$ CMS angular distributions since they are kinematically related. The angular distribution in the $K^+\Sigma^0$ G-J frame (Fig. 9e) tends to be asymmetric, which could be caused by the excitation of nucleon resonances decaying into the $K^+\Sigma^0$ channel [3]. Many of $N^*$ or $\Delta^*$ resonances could contribute to the reaction. All these resonances have large widths and may also contribute through their broad tails to the reaction. The angular distribution of a true two-body resonance reaction is asymmetric only if resonances with both parities are simultaneously excited through interfering amplitudes. Hence, this distribution in the $K^+\Sigma^0$ G–J frame indicates that more than one nucleon resonance with opposite parity participates in the production process [3]. As explained earlier, the $K^+p$ rest frame is equivalent to the rest frame of the exchanged kaon. Therefore, the deviation from isotropy in the $\cos\theta^{FRK^+p}_{p_{b,t},K^+}$ angular distribution could be explained by kaon exchange component [27]. For a pure pion exchange, the Treiman–Yang (T–Y) angle measured in the $K^+\Sigma^0$ rest frame is expected to be an isotropic distribution [34]. Therefore, if a kaon exchange contributes to the production mechanism it should reflect itself in this distribution. The $\Sigma^0$ hyperon T–Y angle measured in the $K^+\Sigma^0$ rest frame, shown in Fig. 10, shows a clear deviation from isotropy, which could be an indication of a significant kaon exchange contribution to the reaction mechanism.
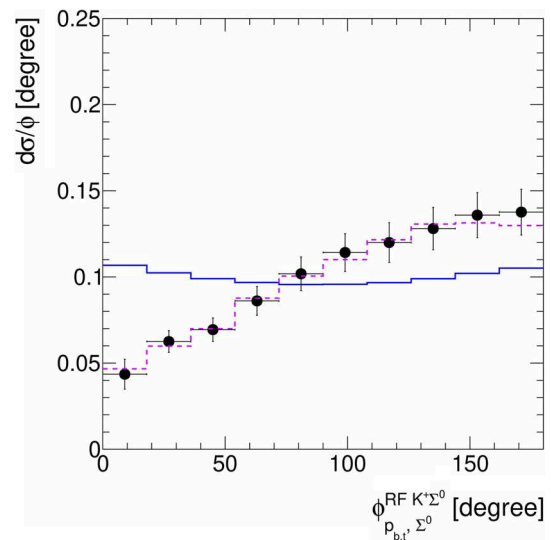


**Fig. 10** The $\Sigma^0$ Treiman–Yang angular distribution measured in the $K^+\Sigma^0$ reference frame. The blue histogram represents the weighted $pp \to pK^+\Sigma^0$ phase space simulation and the dotted histogram indicates the best partial wave analysis solution (discussed in Sect. 6)

## Helicity frames

The helicity angle is defined in a similar way as the G-J angle, but instead of calculating the angle of the respective particle to the initial proton, the helicity angle is calculated between one of the rest frame particles and the third produced particle. The helicity angular distribution thus interrelates the kinematics of the three final state particles and it is thus a linear transformation projection of the Dalitz plot. A uniformly populated Dalitz plot results in isotropic helicity angle distributions. On the other hand, if dynamical effects distort the Dalitz plot, then the helicity angular distribution will be anisotropic. The helicity angular distributions are shown in the bottom row of Fig. 9. All the distributions are significantly non-isotropic, which indicates that the reaction is dominated

**Table 2** Comparison of the normalized Legendre coefficients between the present measurement and the data collected by COSY-TOF experiment at $\epsilon = 162$ MeV [3]

| | $\epsilon = 162$ MeV | | $\epsilon = 556$ MeV | |
|---|---|---|---|---|
| | $A_1/A_0$ | $A_2/A_0$ | $A_1/A_0$ | $A_2/A_0$ |
| $\cos\theta_{\Sigma^0}^{CMS}$ | $0.0 \pm 0.0$ | $0.03 \pm 0.24$ | $0.0 \pm 0.0$ | $0.32 \pm 0.09$ |
| $\cos\theta_{p}^{CMS}$ | $0.0 \pm 0.0$ | $0.25 \pm 0.29$ | $0.0 \pm 0.0$ | $0.43 \pm 0.13$ |
| $\cos\theta_{K^+}^{CMS}$ | $0.0 \pm 0.0$ | $0.48 \pm 0.22$ | $0.0 \pm 0.0$ | $-0.01 \pm 0.1$ |
| $\cos\theta_{p_{b,t},p}^{FRp\Sigma^0}$ | $0.0 \pm 0.0$ | $0.11 \pm 0.15$ | $-0.06 \pm 0.17$ | $0.27 \pm 0.18$ |
| $\cos\theta_{p_{b,t},K^+}^{FRK^+\Sigma^0}$ | $-0.04 \pm 0.04$ | $0.14 \pm 0.18$ | $-0.19 \pm 0.18$ | $0.08 \pm 0.19$ |
| $\cos\theta_{p_{b,t},K^+}^{FRK^+p}$ | $-0.07 \pm 0.07$ | $0.57 \pm 0.18$ | $0.19 \pm 0.12$ | $0.05 \pm 0.26$ |
| $\cos\theta_{p,\Sigma^0}^{FRK^+\Sigma^0}$ | $0.27 \pm 0.27$ | $-0.15 \pm 0.15$ | $0.36 \pm 0.07$ | $-0.08 \pm 0.09$ |
| $\cos\theta_{p,K^+}^{FRp\Sigma^0}$ | $-0.22 \pm 0.22$ | $0.0 \pm 0.15$ | $-0.4 \pm 0.06$ | $0.04 \pm 0.08$ |
| $\cos\theta_{K^+,\Sigma^0}^{FRK^+p}$ | $-0.11 \pm 0.11$ | $0.11 \pm 0.18$ | $0.55 \pm 0.07$ | $-0.11 \pm 0.09$ |

by intermediate resonances. Therefore, an inclusion of intermediate resonances is necessary in order to quantitatively describe experimental angular distributions.

Comparison to lower energy

A comparison of the normalized Legendre coefficients between this measurement and data collected at a lower value of excess energy $\epsilon = 162$ MeV [3] is listed Table 2. The two sets of coefficients show striking differences for few coefficients indicating that the $\Sigma^0$ production mechanism changes between these values of excess energy. The CMS distributions are more forward-backward peaked for the proton and the $\Sigma^0$ hyperon and less peaked for the kaon, pointing to a larger relative contribution of pion with respect to kaon exchange at larger energies. In addition, the helicity angle distributions have a significant asymmetry at the highest energy, in contrast with the lower energy results.

## 5 Total cross section

The total production cross section as function of the excess energy $\epsilon$ is used as a tool to compare the experimental data to the different theoretical approaches. The result on the pp $\rightarrow$ pK$^+\Sigma^0$ production cross section, obtained by integrating the $cos\theta_{\Sigma^0}^*$ angular distribution, is

$$\sigma(pK^+\Sigma^0) = 17.7 \pm 1.7(stat) \pm 1.6(syst) \,\mu b \,.$$

The cross section value is included in Fig. 11, which shows a compilation of the pp $\rightarrow$ pK$^+\Sigma^0$ cross sections as a function of the excess energy. The present data point corresponds to $\epsilon = 556$ MeV, which is depicted by the green square and existed in a region where no other measurements have been performed. This behaviour can not be described by phase
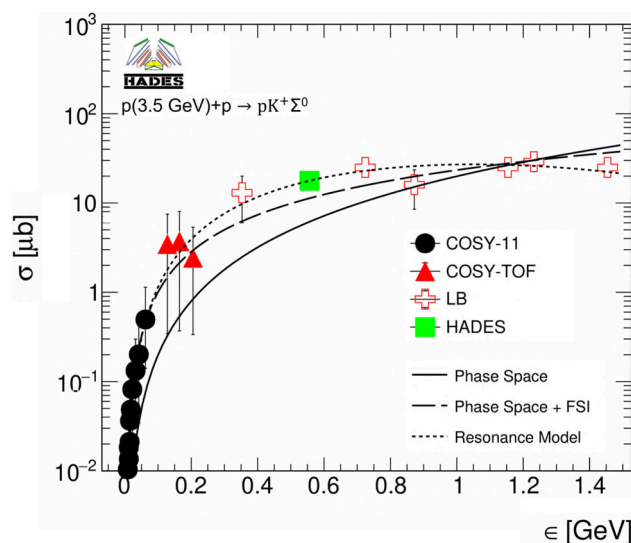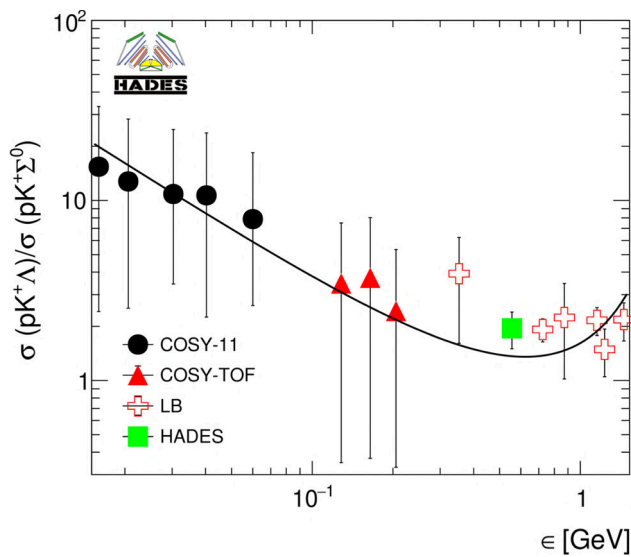


**Fig. 11** Compilation of cross sections of the reaction pp $\rightarrow$ pK$^+\Sigma^0$ from different experiments: COSY-11 [35–40], COSY-TOF [3] and data points from Landolt–Börnstein (LB) [41]. The production cross section of $\Sigma^0$ determined here is shown by the green square. The solid curve represents a pure phase space fit, the dotted curve is a parametrization based on the resonance model and the dashed curve is phase space and FSI as described in the text

space within experimental uncertainty as clearly seen by the solid curve $\sigma_{pK^+\Sigma^0} = K\epsilon^2$, where the quadratic excess-energy dependence is attributed to a pure (i.e. trivial) three-body phase space and $K$ is the fit free parameter.

An alternative parametrization proposed by Fäldt and Wilkin in [42] that takes the proton-hyperon FSI interaction into account

$$\sigma = \frac{C\epsilon^2}{\left(1 + \sqrt{1 + \epsilon/\alpha}\right)^2} \,, \tag{6}$$

where the parameters $C = 7.82 \times 10^2 \,\mu b \, GeV^{-2}$ and $\alpha = 4.57 \times 10^{-2}$ GeV are related to the FSI strength. Interestingly,

**Fig. 12** Experimental cross section ratio of the present data point together with a compilation of the world data: COSY-11 [35–40], COSY-TOF [3] and data points from Landolt–Börnstein (LB) [41]. The present data square is shown by the green square. The solid curve is the ratio of the paramerization of both channels [42,43]

the deviations to the pure phase space behavior start showing up at $\epsilon > 0.2$ GeV. The displayed data in that region could also be approximated by $\sigma \approx 10$ μb.

A more appropriate paramerization proposed by Tsushima in [43] shown by the dotted line is based on a resonance model, where the hyperon is produced via an intermediate nucleon resonance N* or Δ*. This paramerization describes all data points near threshold up to 1.4 GeV fairly well.

Using the pp → pK⁺Λ cross section measured by the HADES collaboration [23], the cross section ratio $\sigma(pK^+\Lambda)/\sigma(pK^+\Sigma^0)$ is determined to be $1.90 \pm 0.41$. Based on the coupled channel calculation, where the interference of the pion and kaon exchange is taken in account, the cross section ratio can be reproduced by selecting the relative sign for these two mechanism [18]. Figure 12 shows the cross section ratio as a function of the excess energy together with a compilation of other measurements [41]. The solid curve is the ratio of the paramerization of both channels, where the paramerization proposed by Fäldt and Wilkin [42] based on phase space and FSI is used for pp → pK⁺Λ and the Tsushima paramerization [43] based on a resonance model is used for the pp → pK⁺Σ⁰ channel.

The observed cross section ratio in the present p+p data is similar to the corresponding value measured in p+Nb data [8], despite the large difference in the individual cross sections, thus corroborating the importance of FSI for these reactions.

## 6 Partial wave analysis

From the results presented above, it was concluded that the experimental data on angular distributions can not be described by pure phase space production, but there must be a resonant component as anticipated in [3]. Therefore, a Partial Wave Analysis (PWA) using the Bonn-Gatchina Partial Wave Analysis (Bo–Ga PWA) framework [44] has been applied with the goal to quantify the relative contributions of different partial waves.

The Bo–Ga PWA framework takes a list of possible transition waves as an input that may contribute to the final state. The non-resonant production proceeds as follows: the proton ($J^P = \frac{1}{2}^+$) and the hyperon (in this case $\Sigma^0$ with $J^P = \frac{1}{2}^+$) are combined into a two particle sub-system and then the kaon ($J^P = 0^-$) is combined with this sub-system to produce the three-body final state. In case of the resonant production, the proton is combined with one of the resonances listed in Table 3 N*-p, or Δ*-p to produce the final state pp → pK⁺Σ⁰. Resonance masses and widths were fixed to the PDG values [45] in order to reduce the number of the free fit parameters.

The strength ($\alpha_1$) and the phase ($\alpha_2$) of each transition wave are determined by fitting the partial wave amplitudes to the experimental data on an event-by-event basis in an unbinned fit. The fit is based on a log-likelihood minimization and the fitting procedure is repeated for many iterations until there is no further improvement of the log-likelihood value. By comparing the log-likelihood value of many fits the best fit can be determined through the largest negative value. As an output, the BG-PWA returns the fitted values of the parameters $\alpha_1$ and $\alpha_2$ and a list of simulated events that have been used as an input but with each event being assigned a weight factor, which gives the contribution of this event to the total yield.

**Table 3** A list of N* and Δ* resonances that might contribute to the pp → pK⁺Σ⁰ reaction. The mass, width and spin-parity quantum numbers were taken from [45]

| Resonance | Mass [GeV$^2$/c$^4$] | Width [GeV$^2$/c$^4$] | J$^P$ |
|---|---|---|---|
| N*(1710) | 1.710 | 0.140 | $\frac{1}{2}^+$ |
| N*(1875) | 1.875 | 0.200 | $\frac{3}{2}^-$ |
| N*(1880) | 1.880 | 0.300 | $\frac{1}{2}^+$ |
| N*(1895) | 1.895 | 0.120 | $\frac{1}{2}^-$ |
| N*(1900) | 1.920 | 0.200 | $\frac{3}{2}^+$ |
| Δ*(1900) | 1.860 | 0.250 | $\frac{1}{2}^-$ |
| Δ*(1910) | 1.900 | 0.300 | $\frac{1}{2}^+$ |
| Δ*(1920) | 1.920 | 0.300 | $\frac{3}{2}^+$ |
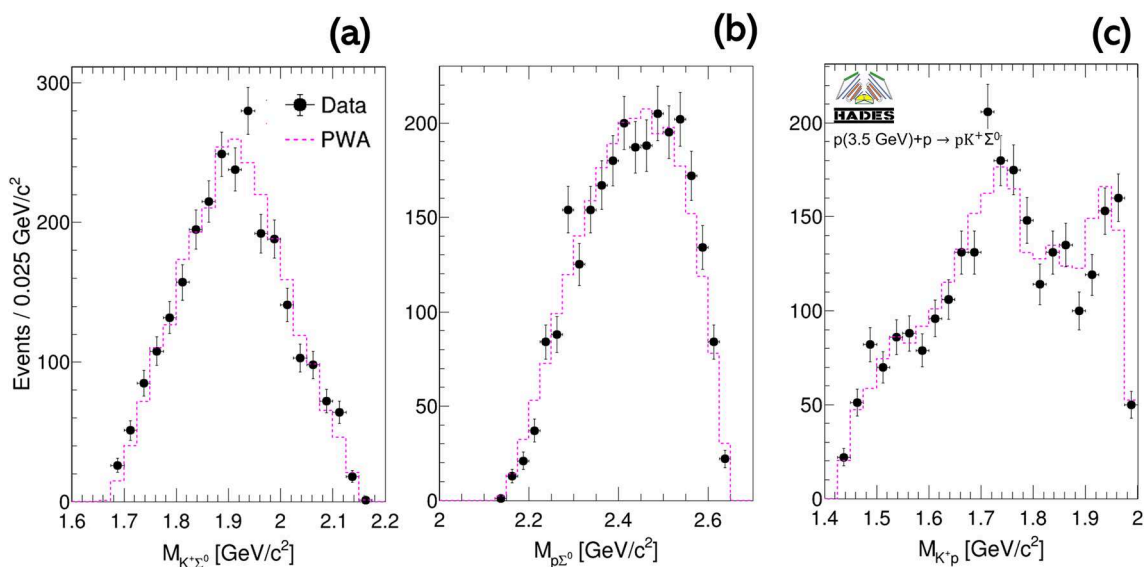
**Fig. 13** Invariant mass spectra of **a** $M_{K^+\Sigma^0}$, **b** $M_{p\Sigma^0}$ and **c** $M_{K^+p}$. The best PWA solution is indicated by the dotted pink histogram

Since the signal region contains background events (mainly $pp \to pK^+\Lambda$ and $pp \to pK^+\Lambda\pi^0$), and because the Bo-Ga PWA method works on an event-by-event basis, it is important to identify whether a particular event belongs to the signal or the background. The $pp \to pK^+\Lambda$ contribution is three times larger than $pp \to pK^+\Lambda\pi^0$ inside the signal region. Therefore, the $pp \to pK^+\Lambda$ channel is considered the main contributing background and its kinematics is modeled by performing a PWA on the $pp \to pK^+\Lambda$ -like events. The solutions published in [23] have been tested and solution No. 8/1 was found to provide the best description of the experimental data by including the p+p initial waves $^{2S+1}L_J = {}^1S_0, {}^3P_0, {}^3P_1$ and $^1D_2$.

The solution No. 8/1 is then applied to the $\Lambda 4\pi$-phase space simulations and these events are filtered through the full simulation and analysis chain. After reconstructing the $\Lambda$ events that have been assigned a PWA weight, the missing mass $MM(pK^+)$ spectrum was investigated and the $\Lambda$ contribution in the signal region $1.170\,\text{GeV}/c^2 < MM(pK^+) < 1.220\,\text{GeV}/c^2$ was determined to be 292 events. Those events are then added to the signal list with a negative weight.

After subtracting the $\Lambda$ contribution, the PWA technique is applied to the $pp \to pK^+\Sigma^0$ events. A systematic variation of the input partial waves was performed and, in addition, the number of non-resonant and resonant final partial waves was varied and the quality of the PWA solution was determined by the negative log-likelihood value of the fit.

The best PWA solution shown by the dashed histograms in Figs. 9 and 10 was obtained by including p+p initial waves $^{2S+1}L_J = {}^1S_0, {}^3P_0, {}^3P_1, {}^3P_2, {}^1D_2$ and $^3F_2$. In addition, nucleon resonances $N^*(1710), N^*(1900)$ and $\Delta^*(1900)$

were found to contribute as well as non-resonant partial waves. However, due to the limited statistics and the large number of free fit parameters, an unambiguous determination of the contributions of each resonance is not possible since these contributions vary significantly for different solutions. Nevertheless, resonances with masses around $1.710\,\text{GeV}^2/c^4$ ($N^*(1710)$) and $1.900\,\text{GeV}^2/c^4$ ($N^*(1900)$ or $\Delta^*(1900)$) are certainly preferred by the fit.

In addition, the best PWA solution provides a good description of the experimental distributions $M_{K^+\Sigma^0}$, $M_{p\Sigma^0}$, and $M_{K^+p}$, as shown in Fig. 13. The $M_{K^+\Sigma^0}$ and $M_{p\Sigma^0}$ invariant mass spectra are sensitive to the mass and width of the included resonances, while the $M_{K^+p}$ invariant mass distribution is primarily determined by detector acceptance, since $K^+p$ cannot be the decay product of a nucleon resonance. However, the $M_{K^+p}$ distribution might potentially indicate the presence of an unknown pentaquark-resonance [3].

## 7 Conclusion and outlook

The exclusive reconstruction of the reaction $pp \to pK^+\Sigma^0$ at a beam kinetic energy of 3.5 GeV has been presented and the $pp \to pK^+\Sigma^0$ total production cross section was determined with an accuracy better than 10% in a region where no data existed. The dynamics of the reaction was investigated by studying the angular distributions in the CMS, G–J and helicity frame. The corrected CMS distributions of the hyperon and the proton show anisotropies that are more pronounced in the case of the proton. This is the expected behavior if the pion exchange mechanism dominates the particle production process in a simple one-boson exchange formalism.

In addition, an investigation of the $\Sigma^0$ T–Y angle measured in the $K^+\Sigma^0$ reference frame, deviates from isotropy, which hints to a non-negligible contribution of the kaon exchange mechanism.

The helicity angular distributions are not isotropic, which indicates that a pure phase space description without momentum-dependent matrix element(s) is by far not appropriate. The influence of different nucleon resonances has been tested by means of a PWA using the Bo–Ga PWA framework. The best solution was obtained by including the initial p+p configurations $^1S_0$, $^3P_0$, $^3P_1$, $^3P_2$, $^1D_2$ and $^3F_2$. Due to the limited statistics, it was not possible to obtain the exact strength of the individual nucleon resonances. However, nucleon resonances N*(1710), N*(1900) and $\Delta$*(1900) are preferred by the fit.

Recently, the HADES setup has been upgraded by an electromagnetic calorimeter (ECAL) and a Forward Detector (FD) based on PANDA experiment straw tubes [46]. The new data that was collected in February 2022 offers the opportunity to perform the same measurement with an upgraded setup at a higher proton beam energy of 4.5 GeV. This upgrade will allow the identification of the daughter photon in $\Sigma^0 \rightarrow \Lambda\gamma$ via the ECAL. In addition, it will improve the mass resolution of the $\Lambda$ hyperon in the FD acceptance and consequently improve the quality of the kinematic refit. Furthermore, the collected data will provide sufficient statistics to extract quantitative contributions of the different nucleon resonances and a measurement of their $K^+\Sigma^0$ branching ratios, which will certainly improve the current measurement.

**Data Availability Statement** This manuscript has no associated data or the data will not be deposited. [Authors' comment: The manuscript has associated data in the HEPData repository (https://www.hepdata. net/).]

## References

1. C.T. Yang, J. Rafelski, Phys. Lett. B **827**, 136944 (2022). https://doi.org/10.1016/j.physletb.2022.136944
2. G.E. Brown et al., Phys. Rev. C **43**, 1881 (1991). https://doi.org/10.1103/PhysRevC.43.1881
3. M. Abdel-Bary et al., Eur. Phys. J. A **46**, 27 (2010). https://doi.org/10.1140/epja/i2010-11023-0
4. J. Adamczewski-Musch et al., Phys. Rev. C **95**, 015207 (2017). https://doi.org/10.1103/PhysRevC.95.015207
5. G. Agakishiev et al., Eur. Phys. J. A **50**, 81 (2014). https://doi.org/10.1140/epja/i2014-14081-2
6. J.T. Balewski et al., Phys. Lett. B **388**, 859 (1996). https://doi.org/10.1016/S0370-2693(96)01360-3
7. R. Münzer et al., Phys. Lett. B **785**, 574 (2018). https://doi.org/10.1016/j.physletb.2018.08.068
8. J. Adamczewski-Musch et al., Phys. Lett. B 781 (2018). https://doi.org/10.1016/j.physletb.2018.02.043
9. G.F. Chew, F.E. Low, Phys. Rev. **113**, 1640 (1959). https://doi.org/10.1103/PhysRev.113.1640
10. J. Sakurai, Nuovo Cim. **20**, 1212 (1961). https://doi.org/10.1007/BF02732532
11. R. Machleidt, K. Holinde, C. Elster, Phys. Rept. **149**, 1 (1987). https://doi.org/10.1016/S0370-1573(87)80002-9
12. R. Machleidt, Adv. Nucl. Phys. **19**, 189 (1989). https://doi.org/10.1007/978-1-4613-9907-0_2
13. S. Abd El-Samad et al., Phys. Lett. B **688**, 142 (2010). https://doi.org/10.1016/j.physletb.2010.03.076
14. A. Sibirtsev et al., Eur. Phys. J. A **27**, 269 (2006). https://doi.org/10.1140/epja/i2005-10268-x
15. A. Budzanowski et al., Phys. Lett. B **687**, 31 (2010). https://doi.org/10.1016/j.physletb.2010.02.082
16. M. Röder et al., Eur. Phys. J. A **49**, 157 (2013). https://doi.org/10.1140/epja/i2013-13157-9
17. S. Abd El-Samad et al., Eur. Phys. J. A **49**, 41 (2013). https://doi.org/10.1140/epja/i2013-13041-8
18. P. Kowina et al., Eur. Phys. J. A **22**, 293 (2004). https://doi.org/10.1140/epja/i2003-10236-6
19. T. Rozek et al., Phys. Lett. B **643**, 251 (2006). https://doi.org/10.1016/j.physletb.2006.07.066
20. A. Sibirtsev et al., Eur. Phys. J. A **29**, 363 (2006). https://doi.org/10.1140/epja/i2006-10097-5
21. J.-J. Xie, H.-X. Chen, E. Oset, Phys. Rev. C **84**, 034004 (2011). https://doi.org/10.1103/PhysRevC.84.034004
22. G. Agakishiev et al., Eur. Phys. J. A **41**, 243 (2009). https://doi.org/10.1140/epja/i2009-10807-5

23. G. Agakishiev et al., Phys. Lett. B **742**, 242 (2015). https://doi.org/10.1016/j.physletb.2015.01.032
24. D.P. Kingma et al., In: Proceedings of the 27th NeurIPS -Volume 2. 3581 (2014). https://doi.org/10.8035-555/2969033-2969226
25. A. Paszke et al., Adv. Neural Inf. Process Syst. **32**, 8024 (2019)
26. I.J. Good, J.R. Stat, Soc. Ser. B **14**, 79 (1952). https://doi.org/10.1111/j.2517-6161.1952.tb00104.x
27. W. Esmail, PhD thesis. Ruhr-Universität Bochum, Fakultät für Physik und Astronomie, Bochum, Germany, Ruhr U., Bochum (2022). https://doi.org/10.13154/294-8563
28. S. Taylor et al., Phys. Rev. C 71 (05), 054609 (2005). https://doi.org/10.1103/PhysRevC.71.054609
29. I. Fröhlich et al., PoS ACAT, 076 (2007). https://doi.org/10.8172-2323/1-050/0076
30. R. Brun et al., CERN-W5013 (1994). https://doi.org/10.17181/CERN.MUHF.DMJ1
31. G. Agakishiev et al., Eur. Phys. J. A **48**, 64 (2012). https://doi.org/10.1140/epja/i2012-12064-y
32. Y. Gal, Z. Ghahramani, ICML2016 48 , 1050 (2016). https://doi.org/10.5555/3045390.3045502
33. K. Gottfried, J.D. Jackson, Nuovo Cim. **33**, 309 (1964). https://doi.org/10.1007/BF02750195
34. E. Ferrari, S. Serio, Phys. Rev. **167**, 1298 (1968). https://doi.org/10.1103/PhysRev.167.1298
35. D. Grzonka, K. Kilian, Nucl. Phy. A **626**, 41 (1997). https://doi.org/10.1016/S0375-8319474(97)00519-8
36. J. Balewski et al., Nucl. Phy. A **626**, 85 (1997). https://doi.org/10.1016/S0375-8349474(97)00524-1
37. J. Balewski et al., Phys. Lett. B **420**, 211 (1998). https://doi.org/10.1016/S0370-8372693(97)01527-X
38. S. Sewerin et al., Phys. Rev. Lett. **83**, 682 (1999). https://doi.org/10.1103/PhysRevLett.83.682
39. S. Abd El-Samad et al., Phys. Lett. B **632**, 27 (2006). https://doi.org/10.1016/j.physletb.2005.09.086
40. Y. Valdau, C. Wilkin, Phys. Lett. B **696**, 23 (2011). https://doi.org/10.1016/j.physletb.2010.11.072
41. H. Schopper, *Landolt-Börnstein New series. Group I 846 Nuclear and particle physics* (Springer, Berlin, 1988). https://doi.org/10.1007/b35211
42. G. Faldt, C. Wilkin, Z. Phys. A 357, 241 (1997). https://doi.org/10.1007/s002180050239
43. K. Tsushima et al., Phys. Rev. C **59**, 369 (1999). https://doi.org/10.1103/PhysRevC.59.369
44. A.V. Sarantsev et al., Eur. Phys. J. A **25**, 441 (2005). https://doi.org/10.1140/epja/i2005-10121-4
45. M. Tanabashi et al., Phys. Rev. D **98**, 030001 (2018). https://doi.org/10.1103/PhysRevD.98.030001
46. J. Adamczewski-Musch et al., Eur. Phys. J. A **57**, 138 (2021). https://doi.org/10.1140/epja/s10050-021-00388-w